Nano Energy 86 (2021) 106054

Contents lists available at ScienceDirect

Nano Energy

journal homepage: http://www.elsevier.com/locate/nanoen

Photocurrent in carbon nanotube bundle: Graded Seebeck coefficient phenomenon

Shen Xu [a,b,1], Hamidreza Zobeiri [b,1], Nicholas Hunter [b], Hengyun Zhang [a], Gyula Eres [c,*], Xinwei Wang [b,*]

[a] Shanghai University of Engineering Science, School of Mechanical and Automotive Engineering, Shanghai 201620, China
[b] Department of Mechanical Engineering, 2025 Black Engineering Building, Iowa State University, Ames, IA 50011, USA
[c] Oak Ridge National Laboratory, Materials Science and Technology Division, Bldg 4100, MS 6118, Oak Ridge, TN 37831, USA

ARTICLE INFO

Keywords:
Graded Seebeck coefficient
Polarized photovoltage
Thermoelectric effect
Carbon nanotube bundle
Structural manipulation

ABSTRACT

Polarized photovoltage of a suspended aligned carbon nanotube (CNT) bundle under uniform optical irradiation is discovered without additional structural modification or bias voltage. Such a phenomenon is very surprising considering the metallic behavior of the overall bundle and zero temperature difference between ends. The photovoltage characteristic time is found similar to the thermal response time under step Joule heating and implies a relation to the thermal behavior of the CNT bundle. A similar thermoelectric voltage is also observed during step Joule heating. Localized laser heating and scanning along the axial direction of the bundle uncovers a linear spatial variation of the local Seebeck coefficient. The Seebeck coefficient linearly decreases from root to tip of the CNT bundle with a rate of a few - $\mu V \cdot K^{-1} \cdot mm^{-1}$. Deep investigation in both the microscopic and macroscopic structures of the CNT bundle reveals that the local alignment of CNT assemblies rather than the minor defects in individual CNTs brings about this linear distribution of Seebeck coefficient in space. The finding presents a new way for direct photon-to-electric energy conversion via Seebeck coefficient grading in CNT structures.

1. Introduction

Since the discovery of carbon nanotubes (CNTs) in 1991 [1], their one-dimensional structure and intriguing electrical and optical properties [1–4] have attracted great attention from the scientific community. Understanding and controlling the physics of the photoresponse of CNTs is critical for their application as photonic devices [5–9]. Since CNTs can be classified as semiconducting and conducting [10], their photoresponse has been attributed to two major mechanisms. One is the photovoltaic effect [11–13], which happens when an external light irradiates semiconducting CNTs. The incident photons will generate electron-hole pairs inside the nanotubes which causes a voltage difference due to the forced separation of electrons and holes under the built-in electric field [10]. The other one is the photo-induced thermoelectric effect [14,15]. The external light source heats the metallic CNTs and introduces a temperature difference across the nanotube. Phonons will propagate due to the temperature gradient and collide with electrons. Thus, a current arises from the collision and movement of these electrons.

Semiconducting single-wall CNTs (SWCNTs) have a direct bandgap and thus the formation of a p-n junction for them is crucial for their applications in electronic, photonic, and optoelectronic applications. Tans et al. [16] first reported the fabrication of a field-effect transistor consisting of one semiconducting SWCNT in 1998. Different polarities between two ends of CNTs causes photocurrent under laser irradiation. He et al. [17] developed a heterogeneous n-p junction using two segments of horizontally aligned SWCNTs with different types of doping and realized a high sensitivity to broadband polarimetry. Freitag et al. [18] fabricated a single-molecule field-effect transistor using a semiconducting CNT, and observed polarization-sensitive photoconductivity of the CNT under infrared laser irradiation when applying a bias voltage between the source and drain. They further reported that the oxygen doping, due to unexpected defects in one end of the CNT, caused differences in the Schottky barriers at the source and drain interfaces, which caused the CNT to respond to laser irradiation even without the bias voltage [19]. Moreover, different doping levels will vary the

* Corresponding authors.
E-mail addresses: eresg@ornl.gov (G. Eres), xwang3@iastate.edu (X. Wang).
[1] These authors contribute equally.

https://doi.org/10.1016/j.nanoen.2021.106054
Received 24 December 2020; Received in revised form 2 March 2021; Accepted 5 April 2021
Available online 14 April 2021
2211-2855/© 2021 Elsevier Ltd. All rights reserved.

thermoelectric properties of semiconducting CNTs. St-Antoine et al. [15] nonuniformly doped a SWCNT film through oxygen desorption under thermal annealing and showed position dependency of local photovoltage characteristics. The spatially distributed Seebeck coefficient-induced photothermal effect was the main reason contributing to the raised photovoltage.

In this work, photovoltage of a pristine vertically aligned carbon nanotube (VACNT) bundle without doping is discovered under a laser irradiation without bias voltage. The combination study using our transient photo-electro-thermal (TPET) and transient electro-thermal (TET) methods further reveals the origin of this phenomenon. A determined slow time constant implies that it results from a thermal effect rather than photovoltaic effect under optical heating. However, a voltage difference should not have occurred across a uniform bundle when its two ends have the same temperature. Under the assumption that there is a nonuniform distribution of local Seebeck coefficient of the bundle, we develop a theoretical model to deduce the local Seebeck coefficient variation along the axis of the VACNT bundle based on the thermoelectric voltage and temperature profile from localized optical heating. The resulting linear distribution in local Seebeck coefficient demonstrates a continuous variation in the structure of the VACNT bundle. Further deep structural investigation uncovers that the order of macroscopic assemblies in the bundle is the main cause for the observed variation in local Seebeck coefficient. Outcomes from this work have implications for controlling the thermoelectrical properties of CNT bulk assemblies through growth manipulation of macroscopic structure to realize photoelectric energy conversion.

2. Photocurrent in VACNT: discovery and transient behavior with polarization

The VACNT bundles used in this work were grown by using the chemical vapor deposition (CVD) method as described in ref. [20]. To be specific, a silicon wafer coated with a catalyst metal layer (composed of 10 nm Al layer and 1 nm Fe layer) is placed in a chamber which is later filled with ferrocene [$Fe(C_5H_5)_2$] and a gas mixture of 2% C_2H_2, 10% H_2, and 88% He at a background pressure of 10^{-7} Torr. The catalyst Fe^{3+} facilitates the growth of C-C bonds, forms a cap, and pushes the cap upward with continuous formation of C-C bonds at the root region. The growth of CNTs finishes at the end of the reaction when the feedstocks stop. The grown CNTs are well vertically aligned as a “forest” on the Si wafer as shown in Fig. 1d. Fig. 1e shows the schematic structure of the CNTs on a Si wafer. The SEM images show details of the sample CNT bundle (Fig. 1a and g) and the two prevailing morphologies of straight and curly shapes in the bundle (Fig. 1a).

The Raman spectrum (532 nm wavelength laser excitation) of the VACNT bundle in Fig. 1c is taken under a 10 × objective with a laser spot diameter of 4.89 μm and an integration time of 10 s. Three pronounced peaks – D peak, G peak, and 2D peak – appear in the Raman spectrum and illustrate the structural quality of the VACNT bundle. The G peak at 1580 cm^{-1} is for the in-plane stretching vibration of the C-C bond in carbonaceous materials referring to the zone center phonons with E_{2g} symmetry. The G peak is slightly broadened by the D′ peak (as shown in Fig. 1d). The D peak at 1350 cm^{-1} is associated with structural disorder including carbonaceous impurities with sp^3 bonding and broken sp^2 bonds in the sidewalls. Such defects are clearly observed in the high-resolution transmission electron microscope (TEM) image of the CNT (Fig. 1b). This TEM image also shows the basal plane is in parallel with the CNT axial direction. Also the high 2D peak at around 2690 cm^{-1} is indicative of the long-range order arising from two-phonon second-order process [21,22].

In our research, a voltage rise over a suspended VACNT bundle after immediate laser irradiation covering the whole sample is occasionally observed. This is very surprising since there is neither temperature nor carrier density difference between its two ends. To deeply investigate the origin of this photoelectric response of the CNT bundle, the transient behavior of this photovoltage is investigated first. Note this photocurrent continuously exists as long as the sample is irradiated with a laser beam. Here the transient study is intended to uncover the characteristic time of such photocurrent upon sudden laser irradiation, in anticipation to uncover its physics origin. Fig. 1f shows one CNT bundle (Sample #1: 2.5 mm length and 37.39 μm wide) connected between two electrodes placed at the root (A) and tip (B). As shown in Fig. 2a, during the experiment, the suspended sample is attached to two separate heat sinks (silicon wafers), and its two ends are connected to external electric wires for voltage monitoring. The silicon wafers could remain attached to the ends of the bundle at room temperature due to their high thermal conductivity of 148 $W{\cdot}m^{-1}{\cdot}K^{-1}$ [23] and relatively large size. Also, silver paste is applied to the joint of the bundle and wire to ensure good electrical and thermal contact. In the measurement (Fig. 2a), a 405 nm laser (B&W Tek Inc.) is employed with a constant emission power of 91 mW. The laser spot size on the bundle is about 2.5 × 3.5 mm^2 and covers the whole length of the sample ensuring laser energy uniformity across the entire sample. The amplitude of the laser beam is modulated with a square wave at a frequency of 5 Hz. The whole setup is housed in a vacuum chamber with a vacuum level less than 2 mTorr to make the convection around the sample negligible.

As shown in Fig. 2b, under this periodic laser irradiation, the sample bundle has an obvious photoresponse voltage that varies from an initial state to a new steady state. Note that there is no external current fed through the sample. Moreover, this photovoltage shows polarization. When the bundle’s A end is connected to the positive electrode, the photovoltage ($\Delta V_{AB}=V_A-V_B$) gradually increases from 0 V in the first 0.1 s when the laser is on. After the laser is off, it returns to 0 V in the next 0.1 s (the blue curve in Fig. 2b). The same voltage measurement is carried out reversing the electrical connection to the sample. The varying trend of the voltage ($\Delta V_{BA}=V_B-V_A$) is opposite (red curve in Fig. 2b). It decreases below 0 V in the first half period and is then back to 0 V in the other half period (laser off). This observation demonstrates that the photoresponse relies on the bundle’s orientation and not the electrical connections and devices since no external current source was involved in the measurement. The overall photovoltage is at the level of ~120 μV, far above the measurement uncertainty and noise level of 0.49 μV.

The photoresponse in Fig. 2b is relatively slow compared to the reported picosecond time range of the photovoltaic process [18]. Thus, it more likely stems from the thermal behavior of the bundle. To further verify this speculation and explore the origin of this physical phenomenon, a transient electro-thermal (TET) experiment is conducted to reveal the thermal evolution of the VACNT bundle. In the TET measurement (as will be detailed in the next section), a square-wave DC current is passed through the sample and the transient voltage change of the sample is measured. Fig. 2e shows the voltage variation during the TET measurement. Based on the constant negative resistance temperature coefficient (RTC) near room temperature, the voltage directly reflects the average temperature rise induced by Joule heating. The evolution of the TET voltage also happens within ~0.1 s. To quantitatively distinguish photon heating and Joule heating the concept of characteristic time, denoted as t_c, is introduced to compare the TET voltage and photovoltage. It is the time for the voltage change to reach 86.65% of the maximum value [24]. t_c is 0.024 s for the TET voltage and 0.026 s for the photovoltage (both laser on and off periods) as shown in Fig. 2c and d. It is interesting to note that these two characteristic times are so close, firmly implying that the voltage variation in the photoresponse is directly related to the temperature rise of the sample and reflects its response to transient optical heating. Therefore, it is possible this response is a result of the thermoelectric effect rather than photovoltaic effect of the VACNT bundle.

3. Photocurrent: its thermal driving force

From the last section, it is shown that the photovoltages in the

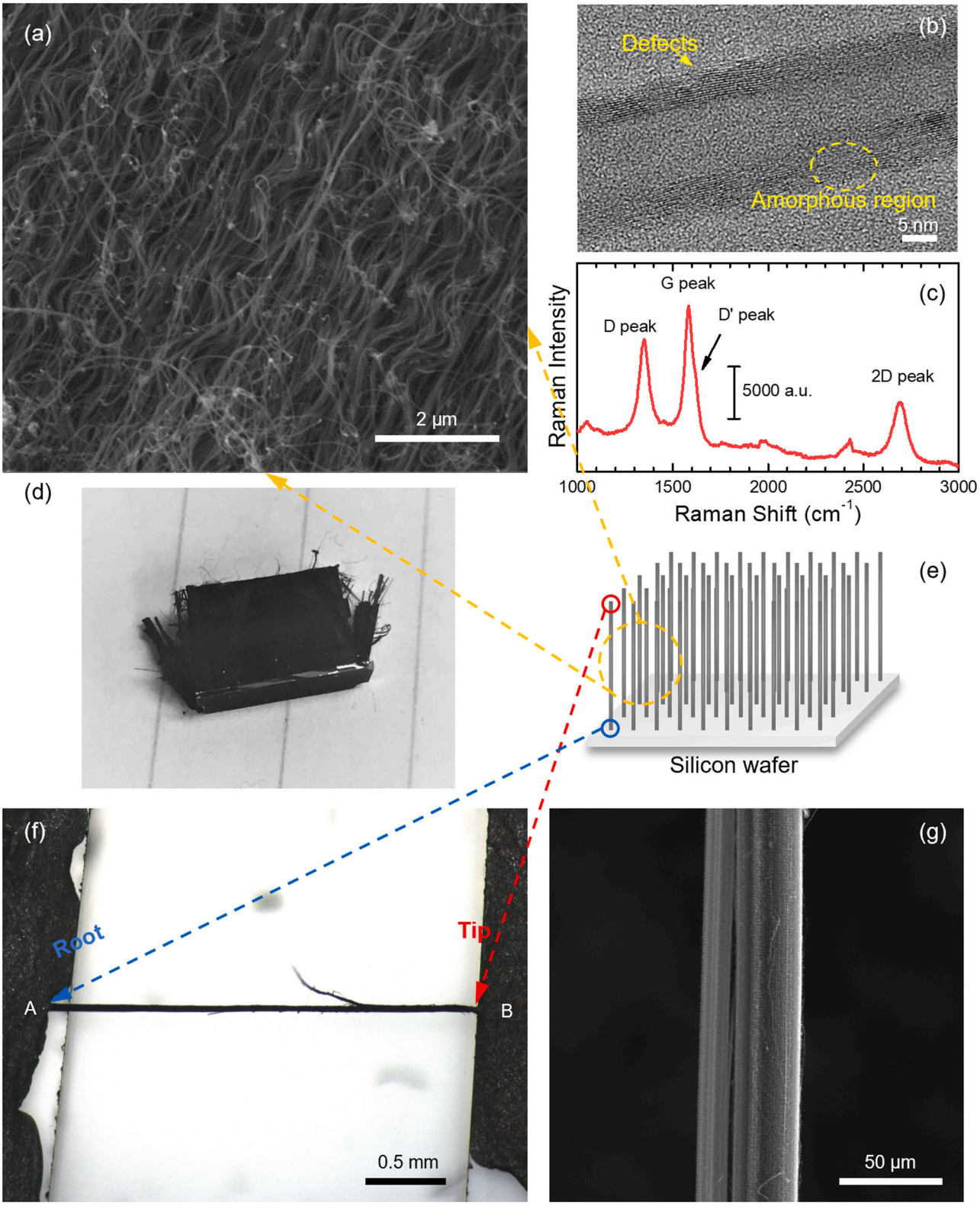

Fig. 1. Structural characterizations of the VACNT bundle. (a) SEM image under 15,000 × magnification showing straight and curly morphologies of individual VACNTs. (b) High resolution TEM image showing defects and amorphous regions in VACNTs. (c) A typical Raman spectrum of the VACNTs. (d) Optical image of VACNTs grown on the silicon substrate. (e) Schematics of the VACNTs grown on Si wafer. (f) Optical image of the VACNT bundle suspended between two electrodes for Sample #1. (g) SEM image under 500 × magnification showing zoom-in details of the VACNT bundle.

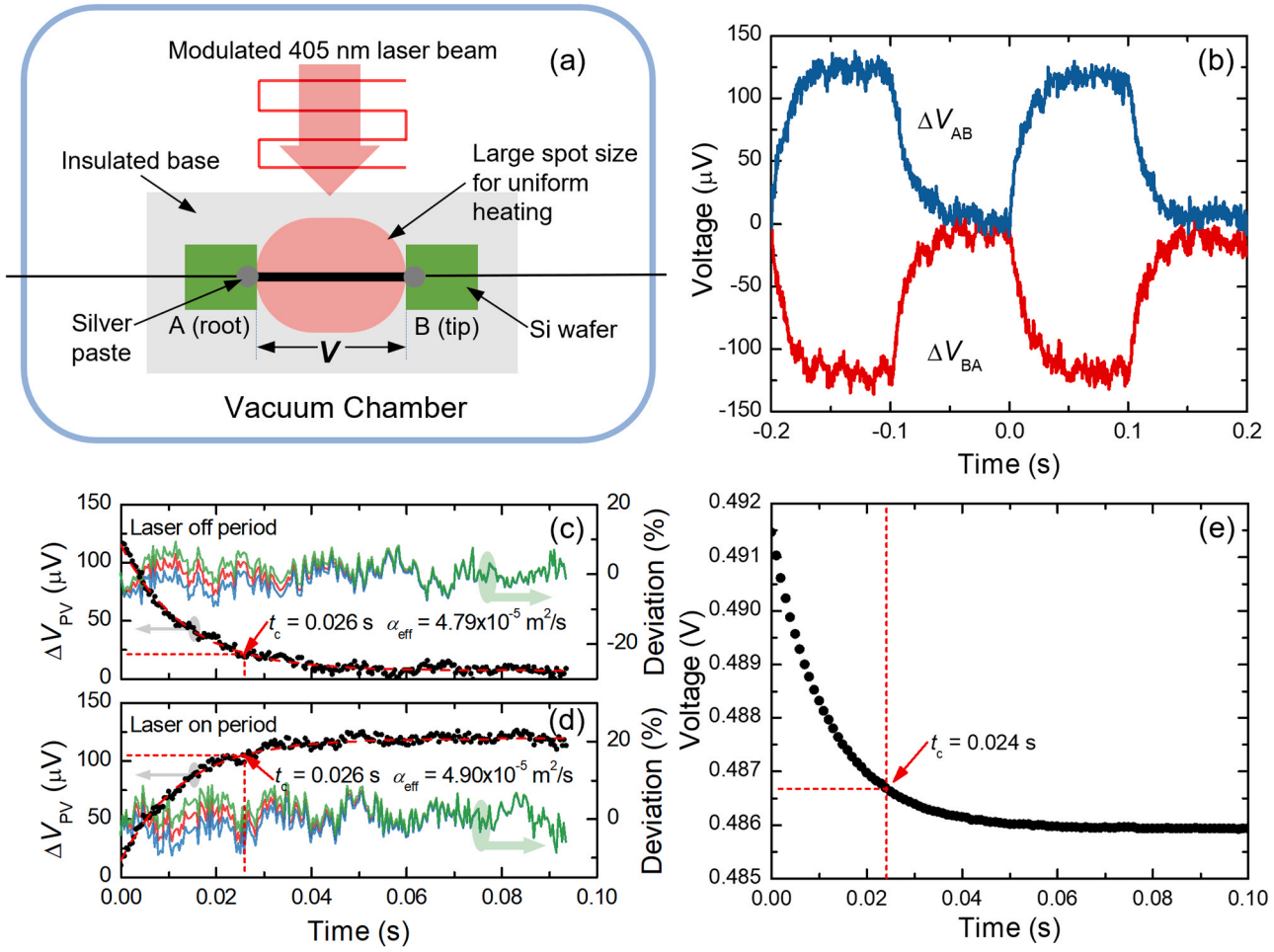

Fig. 2. (a) Schematics of the photovoltage measurement. (b) The photoresponses of the VACNT bundle under periodically modulated laser irradiation for sample #1. ΔV_{AB} ($=V_A$-V_B) is measured with point A connected to the positive electrode and B connected to the negative one. ΔV_{BA} ($=V_B$-V_A) is measured using the reverse electric connections. Analysis of the photovoltage signal for Sample #1 is shown for the (c) laser-off period and (d) laser-on period. For both panels, the original data (black dots) is fitted with a theoretical curve (red dashed line). To the right axis, the percentage of deviation between theoretical voltage [red line based on α_{eff} (effective thermal diffusivity), blue line based on $1.1\alpha_{eff}$, and green line based on $0.9\alpha_{eff}$] and experimental voltage illustrates an uncertainty of α_{eff} better than 10%. The deviation is the difference between modeling and experiment normalized by the overall voltage change. Also, the characteristic time t_c and best fitted α_{eff} are given in each panel. (e) Characteristic time t_c of TET voltage signal during the transient Joule heating process for Sample #1.

sample arising from periodic laser irradiation and step Joule heating have similar time responses. This suggests the photovoltage is induced or related to the temperature rise of the sample rather than the photon-induced charge carrier effect. If such a mechanism does exist, a voltage rise termed the thermoelectric (TE) voltage, for ease of discussion, should be observable under other types of heating, e.g. Joule heating. In this section, the TET technique is used to extract the TE voltage of the sample under Joule heating and develop a better understanding of this phenomena.

The TET technique was first developed by our lab in 2007 [25]. It has been proven to be highly effective in tracing the transient temperature evolution of fiber- or film-like materials and determining their thermal diffusivity with excellent uncertainty (better than ± 5%) [26–29]. The schematic diagram of the TET method is shown in Fig. 3a. Using the same sample, a sudden voltage rise is introduced via Joule heating using a step DC current. Then, the transient temperature response over the bundle is used to determine the thermal diffusivity based on the one-dimensional heat transfer model [25],

$$T^* = \frac{96}{\pi^4}\sum_{m=1}^{\infty}\frac{1-\exp\left[-(2m-1)^2\pi^2\alpha t/L^2\right]}{(2m-1)^4}. \quad (1)$$

It is noteworthy that T^* is a dimensionless temperature rise and is normalized by the steady-state temperature rise under the same Joule heating. It is also a spatially averaged temperature rise rather than a local one as defined in ref. [25]. Besides the thermal diffusivity, this technique can measure the real temperature rise over the sample as it employs the well-defined Joule heating as its heat source. Compared with the voltage/resistance variation resulting from laser irradiation, the TET method can help calculate the temperature rise under laser heating and uncover the physics behind the observed photovoltage phenomenon. However, since the TE voltage (if it exists) is embedded in the overall voltage change of the sample, a bi-directional TET experiment is designed as shown Fig. 3a. The voltage response of the sample under Joule heating from two different current directions could uncover the hypothetical TE voltage.

Fig. 3b and c show the voltage change of the sample under step DC current heating (current: 0.7 mA; modulation frequency: 2 Hz). As shown in the figure, under sudden heating, due to its temperature rise and negative RTC, the voltage (and resistance) experiences a decrease. For the TET result, the 1D heat transfer model fits the voltage signal well, and the determined effective thermal diffusivity (α_{eff}) based on $\Delta V_{B\to A}$ (i.e. current flowing from B to A or V_B-V_A) is 5.19×10^{-5} m^2/s with an uncertainty better than ± 10%. Based on $\Delta V_{A\to B}$ (i.e. with current flowing from A to B or V_A-V_B) the thermal diffusivity is 5.25×10^{-5} m^2/s. As will be discussed later, this tiny difference is

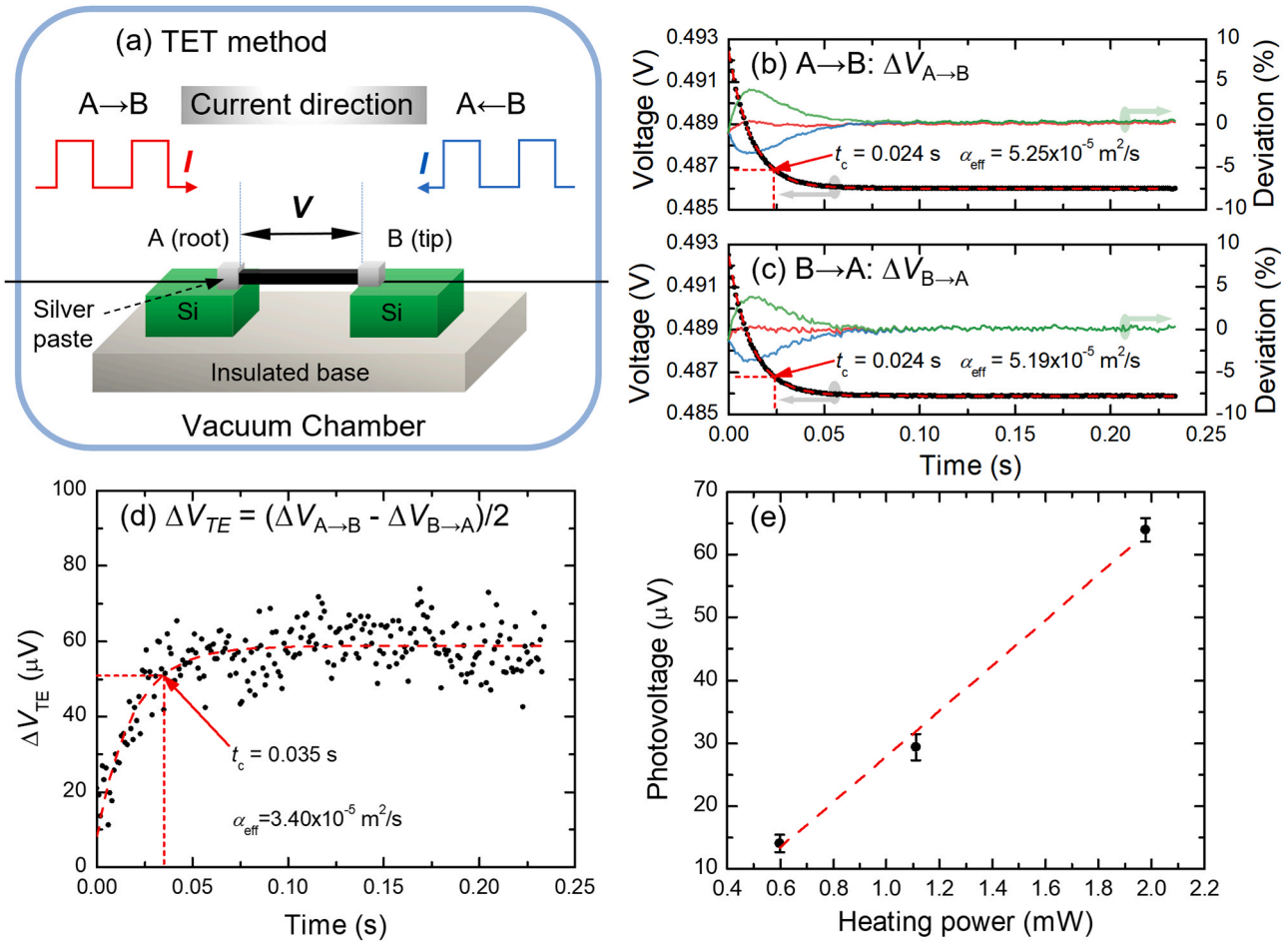

Fig. 3. Thermoelectric effect study on the VACNT bundle for Sample #1 in the TET measurement. (a) Schematics of TET method. Voltage evolution of (b) $\Delta V_{A\rightarrow B}$ and (c) $\Delta V_{B\rightarrow A}$ under Joule heating. The characteristic time t_c and best fitted α_{eff} are shown in the plots. The red dashed line is the best fitting. To the right axis, percentage of deviation between theoretical voltage (red line based on α_{eff}, green line base on $1.1\alpha_{eff}$, and blue line base on $0.9\alpha_{eff}$) and experimental voltage illustrates the uncertainty of α_{eff} better than 10%. The deviation is the difference between modeling and experiment normalized by the overall voltage change. (d) Thermoelectric signal ΔV_{TE} is calculated from subtraction: $(\Delta V_{A\rightarrow B}- \Delta V_{B\rightarrow A})/2$. The red dashed line shows the best fitting using the 1D transient heat transfer model, and the determined t_c and α_{eff} are 0.035 s and 3.4×10^{-5} m^2/s, respectively. (e) The linear relationship between photovoltage and Joule heating power for Sample #4.

induced by the TE voltage embedded in the signal. These results are in good agreement with our pervious results for similar CNT bundles, for example, 1.32–2.96 $\times 10^{-5}$ m^2/s in ref. [21] and 6.1 $\times 10^{-5}$ m^2/s in ref. [30]. For the photovoltage we have obtained, shown in Fig. 2c and d, since we speculate it is related to the temperature of the sample, we also fit the data using Eq. (1) and an effective thermal diffusivity which results in excellent fitting. The determined effective thermal diffusivity turns out to be 4.90×10^{-5} m^2/s for the laser-on period and 4.79×10^{-5} m^2/s for the laser-off period (Fig. 2c and d). These results are very close to the thermal diffusivity of 5.19×10^{-5} and 5.25×10^{-5} m^2/s determined during the TET experiment. It is important to note that the fitting model to determine thermal diffusivities based on photovoltage is reasonable even though we use a 1D heat transfer model to give the average temperature rise. The proof of this statement will be given in the later section. The similar thermal diffusivity resulting from the same theoretical model confirms that the origin of the photovoltage over the VACNT bundle under laser irradiation is a heating effect.

If a TE voltage exists in the measured TET voltage as shown in Fig. 3b and c, we could distinguish it by taking advantage of the directional behavior of the TE response. Such a TE response is calculated as $\Delta V_{TE}= (\Delta V_{A\rightarrow B}-\Delta V_{B\rightarrow A})/2$ and is shown in Fig. 3d. Here a small but distinguishable difference is present between the two voltage curves. Even though the voltage/resistance decrease caused by the temperature rise should be the same for both electrical connection setups, the sign of the TE effect-caused voltage will be different. Thus, subtracting $\Delta V_{B\rightarrow A}$ from $\Delta V_{A\rightarrow B}$ excludes the TET signal while the sole TE signal ΔV_{TE} remains (Fig. 3d). We also try to fit this ΔV_{TE} using the 1D heat conduction model Eq. (1) to see the level of thermal diffusivity it can uncover. Since ΔV_{TE} is very weak and larger noise arises from subtraction, the determined effective thermal diffusivity of 3.40×10^{-5} m^2/s is a little lower than the one from the TET signal (5.19×10^{-5} m^2/s) but is still in the same magnitude. The physics behind this difference will be explained in a later section. Up to this point, we can conclude that the small difference in the determined α_{eff} by $\Delta V_{A\rightarrow B}$ and $\Delta V_{B\rightarrow A}$ is caused by the TE signal embedded in the TET voltage response.

Fig. 3e shows the TE voltage variation against the Joule heating power for another sample we have tested (Sample #4 detailed in

Table 1
Summary of length, width, effective thermal diffusivity α_{eff}, characteristic time t_c determined from TET signal and photovoltage signal, respectively, and photovoltage $\Delta V_{PV,s}$ for all four samples.

Sample #	Length (mm)	Width (mm)	α_{eff} (m^2/s)	t_c (s)		$\Delta V_{PV,s}$ (μV)
				ΔV_{TET}	ΔV_{PV}	
1	2.508	0.037	5.19×10^{-5}	0.024	0.035	120.9
2	0.798	0.152	1.28×10^{-5}	0.010	0.0083	19.5
3	1.016	0.080	2.82×10^{-5}	0.007	0.010	42.9
4	0.898	0.195	3.36×10^{-5}	0.005	0.012	324.4

Table 1). The TE voltage shows an excellent linear relation with the heating power. Since the sample's temperature rise is proportional to the Joule heating power, we can conclude that the TE voltage is linearly related (proportional) to the sample's temperature rise. By studying the time response and magnitude of the voltage signal, it is concluded that the temperature rise of the sample caused by photon heating does indeed induce the photovoltage.

4. Physics of photovoltage: Seebeck coefficient grading

One intriguing observation is the photovoltage over this VACNT bundle is nonzero under uniform optical heating when its two ends have the same state (no temperature difference or different densities of state). In the above section, we proved that the photovoltage is a thermoelectric effect (thermally induced voltage rise). If the CNT bundle has a constant Seebeck coefficient S along the axial direction, there should be no voltage over the bundle under either photon or Joule heating. So here S should be nonuniform along the axial direction of the bundle. To further explore this idea and quantitatively evaluate the local S, we set up an experiment: transient photo-electro-thermal (TPET) technique with bi-direction voltage detecting with focused laser heating. The (TPET) technique [24] was first developed in our lab for measuring the thermal diffusivity of micro/nanoscale fiber-like materials. The bi-directional TPET technique is shown in Fig. 4a. The sample bundle is irradiated by a square-wave modulated laser which works as a heating source through photon absorption and results in a temperature rise in the sample [25]. Meanwhile, a DC current goes through the bundle to record the varying temperature-dependent resistance as a voltage signal. After the laser is on, one-dimensional heat conduction immediately occurs along the axial direction of the sample due to the temperature difference between the heating point [30] and the heat sinks. Based on the negative RTC of carbon material around room temperature, the voltage over the CNT bundle will decrease to a lower level. Thus, in the TPET experiment, the focused and localized incident laser will cause both the above-mentioned photovoltage and transient voltage decrease due to temperature rise (resistance decrease). However, the photovoltage is polarized (detailed later) while the latter is not. Thus, based on this distinct feature, we can distinguish these two effects easily by using bi-directional current feeding and sensing following the same methodology in the bi-directional TET measurements.

In the experiment, the laser spot is focused to a smaller size so that only a small portion of the CNT bundle is directly heated by the laser. The exact location of the heating point (the highest temperature location) can be well-defined in this method. As the laser is scanning along the sample bundle we produce two different temperature gradients on both sides of the heating point to further study its TE response and investigate the physics behind this phenomenon.

4.1. Variation of temperature rise and photovoltage against laser spot location

The laser spot is reshaped and focused to a line shape with a narrow width of 0.4 mm as shown in Fig. 4a. The long axis of the laser spot is perpendicular to the axial direction of the sample bundle. A low DC current of 0.7 mA is applied to the bundle to measure the overall thermal response during laser scanning. The obtained voltage change reflects the change in electrical resistance due to temperature rise. It includes two effects: one from photovoltage ΔV_{PV} and the other from optical heating-induced resistance change ΔV_{TPET}. Since ΔV_{PV} is polarized but ΔV_{TPET} is not, they can be separated by using the same data processing method from the TET measurement. We define the voltage over electrode A to electrode B as the photovoltage signal and calculate it as $\Delta V_{\mathrm{PV}} = (\Delta V_{\mathrm{A}\to\mathrm{B}}\text{-}\Delta V_{\mathrm{B}\to\mathrm{A}})/2$. $\Delta V_{\mathrm{A}\to\mathrm{B}}$ and $\Delta V_{\mathrm{B}\to\mathrm{A}}$ are the overall voltages under laser heating when the external current flows from A to B, and from B to A. $\Delta V_{\mathrm{PV,s}}$ is defined as the maximum voltage change in ΔV_{PV} from the initial state to steady state.

Besides ΔV_{PV}, the temperature rise is another important parameter for S determination. The resulting ΔV_{TPET} can be used to calculate $\Delta\overline{T}$ based on the calibrated RTC for Sample #1. To eliminate the effect of TE voltage on temperature evaluation, ΔV_{TPET} is calculated as $V_{\mathrm{TPET}} = (\Delta V_{\mathrm{A}\to\mathrm{B}}+\Delta V_{\mathrm{B}\to\mathrm{A}})/2$. The average temperature rise of the sample is calculated as $\Delta\overline{T} = (\Delta V_{TPET,\infty} - \Delta V_{TPET,0})/I/(dR/dT)$, where $\Delta V_{TPET,\infty}$ and $\Delta V_{TPET,0}$ are the final and initial V_{TPET}, and I is the electrical current. When considering a constant thermal conductivity for the bundle in the transient measurement, the maximum temperature rise $\Delta T_{\max}$ (at the laser heating location) is twice that of $\Delta\overline{T}$. The calibration of RTC (dR/dT) is carried out in our cryogenic system (JANIS). The bundle is put on a cold finger which conducts heat away from the bundle during cooling. A thermistor is installed inside the cold finger to accurately monitor the temperature. The exact resistance of the bundle is measured in a vacuum (0.4 mTorr) from 300 K to 195 K with a temperature step of 15 K. A 30-minute interval between each measurement ensures the sample reaches the targeted temperature. The measured resistance shows a good linear response to temperature and the RTC is finally determined to be $-0.691\ \Omega\cdot\mathrm{K}^{-1}$ for Sample #1.

With a scanning step of 0.08 mm, the transient behavior of ΔV_{TPET} and ΔV_{PV} are shown in contour maps in Fig. 4c and e. Fig. 4d and f exhibit four typical voltage curves at different locations. It is clear that when the laser spot is close to the sample end, the included ΔV_{TPET} and ΔV_{PV} are very small (close to zero). This is due to the very small thermal resistance from the laser heating location to the electrodes and the subsequent small temperature rise. The resulting $\Delta V_{\mathrm{PV,s}}$ and $\Delta\overline{T}$ are shown in Fig. 4g and h against the laser spot location. Both $\Delta V_{\mathrm{PV,s}}$ and $\Delta\overline{T}$ share a similar variation trend and have a low value when the laser spot is at two ends of the bundle. This is because the total thermal resistance from the laser heating location to the two ends parabolically varies when the heating point is moving along the axial direction. Since the bundle has a large aspect ratio (length to diameter), the heat conduction in the bundle can be treated as one dimensional. Also, the heat convection is negligible in vacuum. The heat radiation is also negligible as the temperature rise over the sample is low ($\Delta\overline{T} \sim 10$ K). When the laser irradiates at location x as shown in Fig. 4a, the generated heat immediately dissipates to two ends of the bundle (heat sinks) after a temperature gradient is established. The network of thermal resistance is shown in Fig. 4a. $R_{t,0\text{-}x}$ and $R_{t,x\text{-}L}$ are in parallel, and at steady state the total thermal resistance of the bundle is $R_t = x(L-x)/(kAL)$, where A and L are the cross-sectional area and length of the bundle. Since the incident power is constant and its location x varies, the maximum temperature rise $\Delta T_{\max}$ is proportional to R_t and is a parabolic function of x as $q_x\cdot x(L-x)/(kAL)$, where q_x is the constant heat transferring rate. When the laser spot is at the two ends of the bundle, the thermal resistance is very low and will only cause a small temperature rise. Thus, the thermoelectric effect that depends on the temperature rise is also weak and produces a low photovoltage. When the laser spot moves to the middle of the bundle, the heat dissipation experiences larger resistances and raises the temperature more which leads to a higher photovoltage over the bundle. As shown in Fig. 4g and h, the shape of ΔV_{PV} and $\Delta T_{\max}$ against x deviates from the parabolic function a little bit. This is caused by the non-uniform structure of the sample along the axial direction, which could have some effects on laser absorption and thermal conductivity. To be specific, the temperature rise is higher when the laser spot is on the side closer to the sample root. This will be explained by the structure-induced thermal conductivity variation in Section 6.

4.2. Seebeck coefficient grading

The speculation that the Seebeck coefficient S along the axial direction is not constant can be expressed as $S(x) = S_0 + S_x$, where S_0 denotes the constant portion, and S_x is a position-related variable based on the reference value of S_0 and has $\int_0^L S_x dx = 0$. Note such a breakdown of S has no effect on the generated photovoltage over the bundle and is

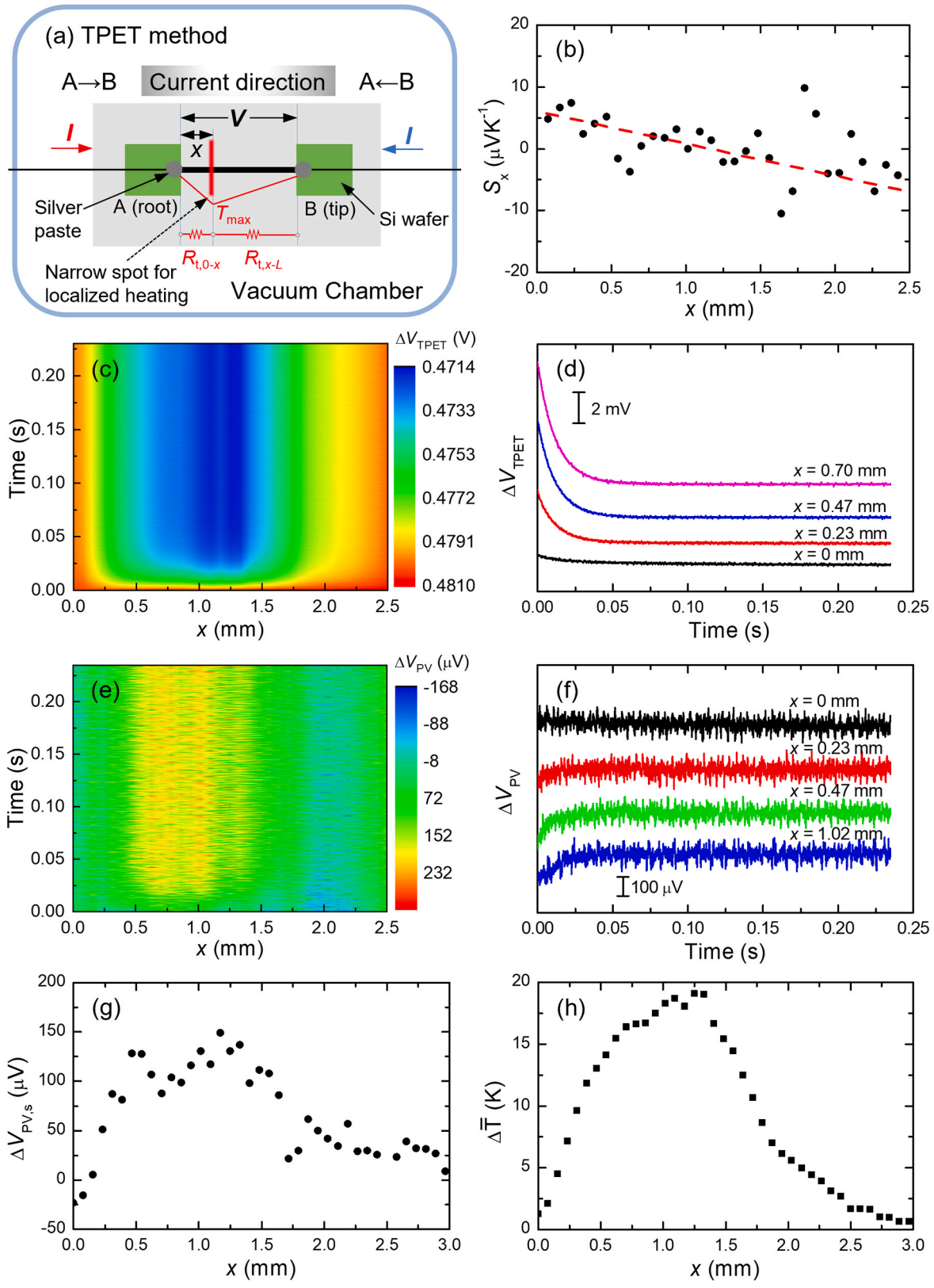

Fig. 4. Study on photovoltage under localized laser heating for Sample #1. (a) Schematics of the scanning TPET measurement. (b) The relative Seebeck coefficient S_x as a function of x (the laser spot position relative to its root end A). The dashed line is a linear fitting to show the varying trend of the data. (c) 2D contour map of TPET voltage [$\Delta V_{TPET} = (\Delta V_{AB} + \Delta V_{BA})/2$] against time and location of the laser heating point. (d) Four voltage curves at selected locations of Fig. c. (e) 2D contour map of photovoltage [$\Delta V_{PV} = (\Delta V_{AB} - \Delta V_{BA})/2$] against time and location of laser heating point. (f) Four photovoltage curves at selected laser heating locations. (g) The maximum photovoltage variation with the laser heating location. (h) Average temperature rise of the sample against the laser heating location.

only for the ease of physics analysis. Only S_x contributes to the observed photovoltage. Given that $\Delta V_{PV,s}$ is the voltage measured from electrode A to electrode B, we define the origin of the coordinate at point A in Fig. 4a. Thus, the voltage $\Delta V_{PV,s}$ can be expressed as

$$\Delta V_{PV,s} = \int_A^x S_x dT_1(x) + \int_x^B S_x dT_2(x), \quad (2)$$

in which L is the bundle length, x is the location of the laser, and $T_1(x)$ and $T_2(x)$ are the temperature distributions in the ranges of point A to x and x to point B. In the heat transfer model for the fiber under irradiation of a focused laser, heat conducts along the axial direction of the fiber while the thermal convection and thermal radiation are negligible in the vacuum chamber. Both temperature distributions have a linear profile against the location, with constant $T_1'(x) = dT/dx|_{A\sim x} 2\Delta\overline{T}/x$ and $T_2'(x) = dT/dx|_{x\sim B} = -2\Delta\overline{T}/(L-x)$ when the thermal conductivity is assumed constant along the bundle which is physically reasonable for our case. Then we rearrange Eq. (2) to be

$$\Delta V_{PV,s} = [T_1'(x) - T_2'(x)] \int_0^x S_x dx + T_2'(x) \int_0^L S_x dx. \quad (3)$$

Since we have $\int_0^L S_x dx = 0$, a simple expression between the relative Seebeck coefficient S_x and other known physical properties (including the voltage, temperature rise, and location) is derived as

$$S_x = \frac{dV_{PV,s}}{dx} \Big/ \left(Q_{abs} A k\right) \quad (4)$$

Note Eq. (4) is applicable when the laser absorption Q_{abs}, A, and k are constant. Such a strict condition does not apply to our case, so S_x needs to be solved numerically based on the measured $\Delta V_{PV,s}$ and $\Delta\overline{T}$. With the photovoltage and temperature rise shown in Fig. 4g and h, the determined relative Seebeck coefficient against the location is presented in Fig. 4b. It shows a linear decrease from 7 $\mu V \cdot K^{-1}$ to − 7.5 $\mu V \cdot K^{-1}$ with a changing rate of − 3.3 $\mu V \cdot K^{-1} \cdot mm^{-1}$ from root to tip. Also, with this linear S_x-x relation, the dependence of $\Delta V_{PV,s}$ on $\Delta\overline{T}$ can be easily verified by using the integral of $\Delta V_{PV} = \int_0^L S_x dT$. Tian et al. [31] prepared macroscopic bundles consisting of MWCNTS using the normal carbon arc plasma method and measured the thermoelectric power of the bundle to be around 23 $\mu V \cdot K^{-1}$ at room temperature. Later, Kim et al. [32] suspended a single MWCNT on a microfabricated device and reported its room temperature Seebeck coefficient to be 80 $\mu V \cdot K^{-1}$. Miao et al. [33] reported the Seebeck coefficient of an individual MWCNT ranges from 29.4 to 41.0 $\mu V\ K^{-1}$ and decreased against increased temperature. The lacking of tube-tube junctions in the single MWCNT may attribute to the increase in the Seebeck coefficient of the single MWCNT when compared with the previous synthesized macroscopic MWCNTS bundle.

As a semiconductor with a direct bandgap, many effects have been explored for tuning the thermoelectric properties of CNTs, especially for SWCNTs, widely from positive value to negative value by using either p-type doping or n-type doping. Nonoguchi et al. [34] doped SWCNTs with different organic dopants and observed variation of the Seebeck coefficient from + 90 $\mu V \cdot K^{-1}$ to − 80 $\mu V \cdot K^{-1}$. Nakai et al. [35] reported a large variation in Seebeck coefficient by doping a semiconducting SWCNT film with different concentrations of metallic SWCNTs, claiming that thermally resistive junctions between SWCNTs accounted for the variations. The work by MacLeod et al. [36] showed an increase in Seebeck coefficient by synthesizing composite polymers with SWCNTs. Chakraborty et al. [19] summarized the variation of Seebeck coefficients from − 100 $\mu V \cdot K^{-1}$ to 150 $\mu V \cdot K^{-1}$ of CNTs with different dopants in their review work. St-Antoine et al. [15] applied current conditioning to a suspended SWCNT film to form a symmetric doping which resulted in an unevenly space-distributed Seebeck coefficient with a relative variation range of 20 $\mu V \cdot K^{-1}$ in a 2 mm long CNTs film through partially desorbed redox active species in the CNTs. Thus, structural defects and doping level might be the reason behind the variation of the local Seebeck coefficient. Although the absolute Seebeck coefficient of our sample is not measured here, the variation of Seebeck coefficient is determined and its varying range is in reasonable accordance with literature [15,19]. Our observed graded Seebeck coefficient-induced photocurrent phenomenon prompts a novel way to directly convert photon energy to electricity. The conversion efficiency is still very low for our CNT samples since their structure is not optimized for such conversion. Since the measured photovoltage (ΔV_{PV}) is under open circuit condition, the maximum power output will be $\Delta V_{PV}^2/(4R)$ with matched load impedance where R is the sample's resistance. The conversion efficiency of Sample #1 is estimated as 5.4×10^{-9}. Note this is for the case that the sample has a temperature rise of only 10 K where the ideal efficiency (Carnot efficiency) is only 3.3%. The conversion efficiency can be improved by reducing the electrical resistance of the sample via electric current annealing [21]. One very critical way to improve the efficiency is significantly increasing the Seebeck coefficient gradient along the sample. For instance, half of the sample can be made p-doped and the other half is n-doped [34]. In this way, the conversion efficiency can be increased by several orders of magnitude. The Seebeck coefficient gradient-induced phenomenon opens a new way for direct photon-to-electric energy conversion. Such idea can be applied to high-efficiency thermoelectric materials (e.g. AgPbSbTe type of materials) to realize compelling direct photon-to-electric energy conversion.

5. Seebeck coefficient grading: synthesis-induced structural effects

The strong linear variation in the Seebeck coefficient along the VACNT bundle suggests that its structure or composition may be non-uniform. Such S distribution/photocurrent effect may arise from the growing mechanisms of our VACNTs. If it is true, then all the other CNT bundles in the same synthesis batch should have a similar photoresponse when photon irradiation is applied. Thus, we test three sample bundles which are randomly selected on the same silicon wafer. All three samples show the similar photoresponse and the same trend as the previous sample bundle. The optical images and photoresponse of the samples are shown in Fig. 5. "A" denotes the root end of the VACNT bundles and "B" is for the tip end. Fig. 5d and e show the transient photovoltages of three samples (Sample #2-#4) under amplitude modulated laser irradiation. The same directional trend is observed for all four samples which reflects the photovoltage resulting from the VACNT structure. Sample #2-#4 have a similar, but smaller time t_c compared with Sample #1 because they are shorter in length. Out of the four samples studied in this work, Sample #1 and #4 have very high photovoltages at the level of 100 μV while Sample #2 and #3 have smaller values around 10 μV. The differences in absorption of the incident light, the sample cross-section area, and sample length all will affect the temperature rise, which in turn affect the overall photovoltage magnitude. Additionally, the difference in samples' intrinsic S variation with location could also affect the overall photovoltage magnitude.

Table 1 summarizes four samples' geometry, thermal diffusivity, characteristic time under Joule heating, $\Delta V_{PV,s}$, and characteristic time of the photovoltage. It is evident Sample #2-#4's photovoltage characteristic time, although close to that of the time found during TET testing, shows some difference. The characteristic time of the TET testing reflects the average temperature rise behavior. For the photovoltage $\Delta V_{PV} = \int_0^L S_x dT_1(x)$, if S_x follows an exactly linear relation with location x as $S_x = a + bx$, then it is easy to prove that $\Delta V_{PV} \propto \Delta\overline{T}$. Under such conditions, the $\Delta V_{PV} \sim t$ curve will have the same characteristic time as the $V_{TET} \sim t$ curve. If the linear relation $S_x = a + bx$ deviates, then the $\Delta V_{PV} \sim t$ curve will have a characteristic time different from that of the $V_{TET} \sim t$ curve. The results summarized in Table 1 exactly reflect such a scenario.

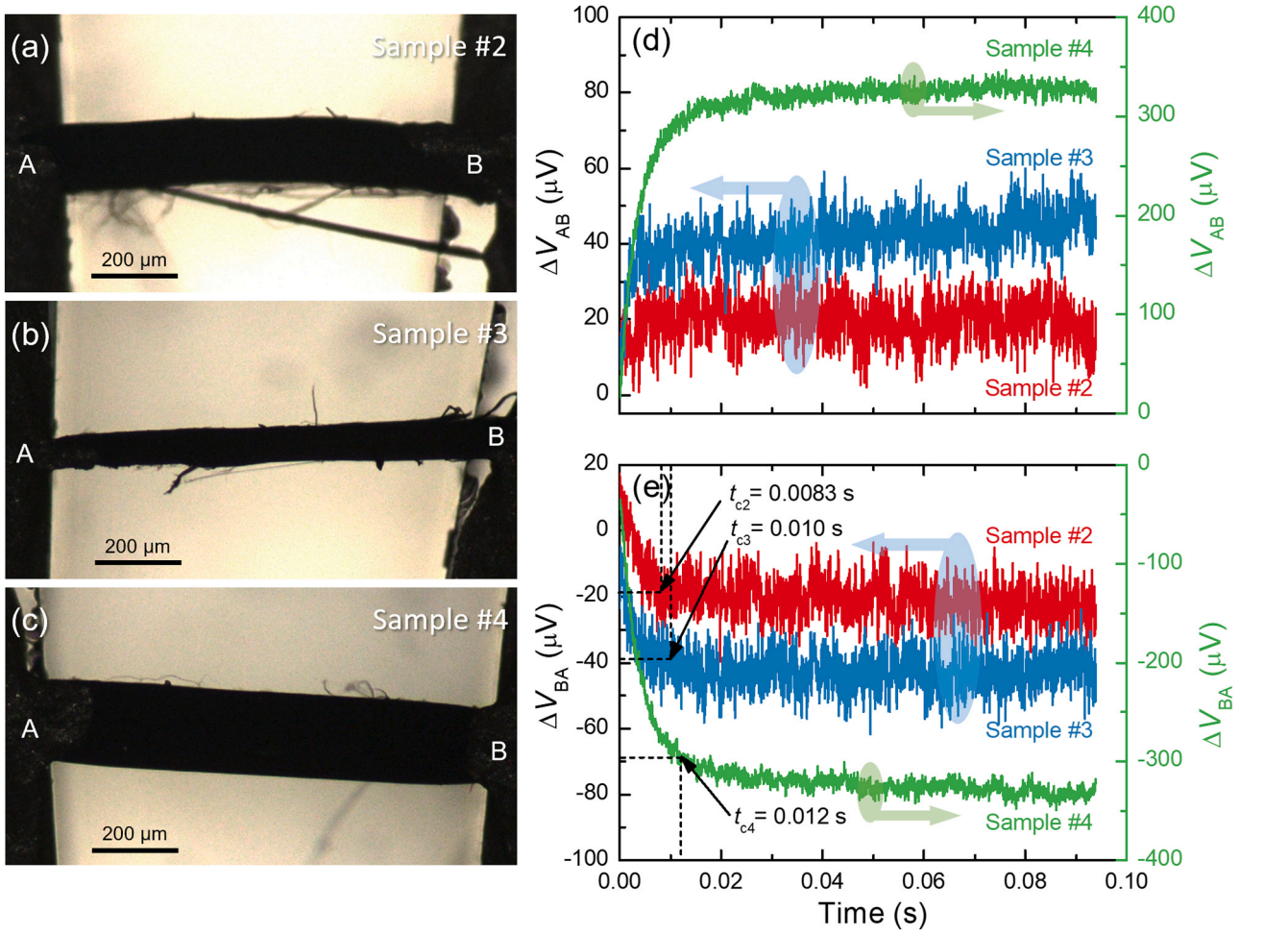

Fig. 5. Another three VACNT bundles were randomly selected from the same batch for photovoltage study. (a)-(c) show the optical images of Samples #2-#4. The transient photovoltages of the samples measured in two directions under laser heating are given in (d) for ΔV_{AB}, and (e) for ΔV_{BA}. The characteristic times of the three samples' photovoltage response are also shown in Fig. (e).

6. Structure behind Seebeck coefficient grading

To further explore the physics behind Seebeck coefficient grading along the sample's axial direction, we investigate the structural details of the VACNTs using scanning Raman spectroscopy. A series of Raman spectra are collected with a spatial step of 0.05 mm along the VACNT bundle along the same scanning direction as that in the photoresponse study for Sample #1 (Fig. 6a). Three main peaks of D, G, and 2D are present in all Raman spectra (Fig. 6b for Raman mapping) and the sequentially selected Raman spectra are shown in Fig. 6c. In Fig. 6b, the change in intensity of D, G, and 2D peaks are obvious. A little enhancement exists for D peak, while the intensity of both G and 2D peaks decreases when x increases. Additionally, Fig. 6c supplements the intensity variation by showing the gradual broadening of G peak due to D′ peak. The Raman results illustrate a better crystalline structure in the root region. Fig. 6d and e show the intensity ratio evolution for D peak to G peak and 2D peak to G peak along the bundle from root to tip. The intensity ratio of D peak to G peak reveals information about the quality of the bundle: the decreasing trend [21,37–39] along the scanning direction illustrates a lower defect level in the root region than in the tip region. Furthermore, a higher intensity ratio of 2D peak to G peak in the region close to the root confirms long-range order in this region [40,41]. Both ratios substantiate the fact that the root region has better structure than the tip region.

The systematic kinetic study of autocatalytic polymerization in ref. [43,44] elucidates the growing process of the VACNTs used here. The onset of VACNTs growth occurs after the decomposition of the Fe $(C_5H_5)_2$ precursor which provides catalytically active α-Fe_2O_3 [45] and active sites for nucleation for the CNTs on the predeposited catalyst film. Accompanied by H abstraction and acetylene addition, five- or six-membered adducts cyclizes to form a 'CNT cap' from the feedstock of C_2H_2. Then, dehydrogenation at the rim of the 'cap' continuously offers new active carbon radical sites and facilitates the growth of sidewalls of CNTs from the catalyst film. In a small period at the beginning of VACNTs growth, though acetylene polymerization would accelerate the polymerizing speed with the help of water and metallic oxide, it favors random chain propagation rather than cyclization. Instead, metallocene intermediates produces from the thermal decomposition of $Fe(C_5H_5)_2$ interacts catalytically with C_2H_2 to promote the formation of aromatic carbon species and to facilitate ordered structure growth in VACNTs. Thus, the local structure of VACNTs improves as the chemical reaction progresses. Our Raman results are consistent with their findings that the root portion has fewer defects than the tip portion in individual VACNTs due to the bottom-up growing process.

However, this nanoscale structural quality evolution of individual VACNTs could not account for the varying trend of the local Seebeck coefficient along the length direction because amorphous carbon (a-C), regarded as the main defect in the VACNTs, has been reported to exhibit p-type doped semiconducting behavior [46]. It would increase the local Seebeck coefficient rather than decrease S as shown in Fig. 4b. Other factors like macroscopic alignment of nanotubes need to be evaluated to explain the Seebeck coefficient grading effect.

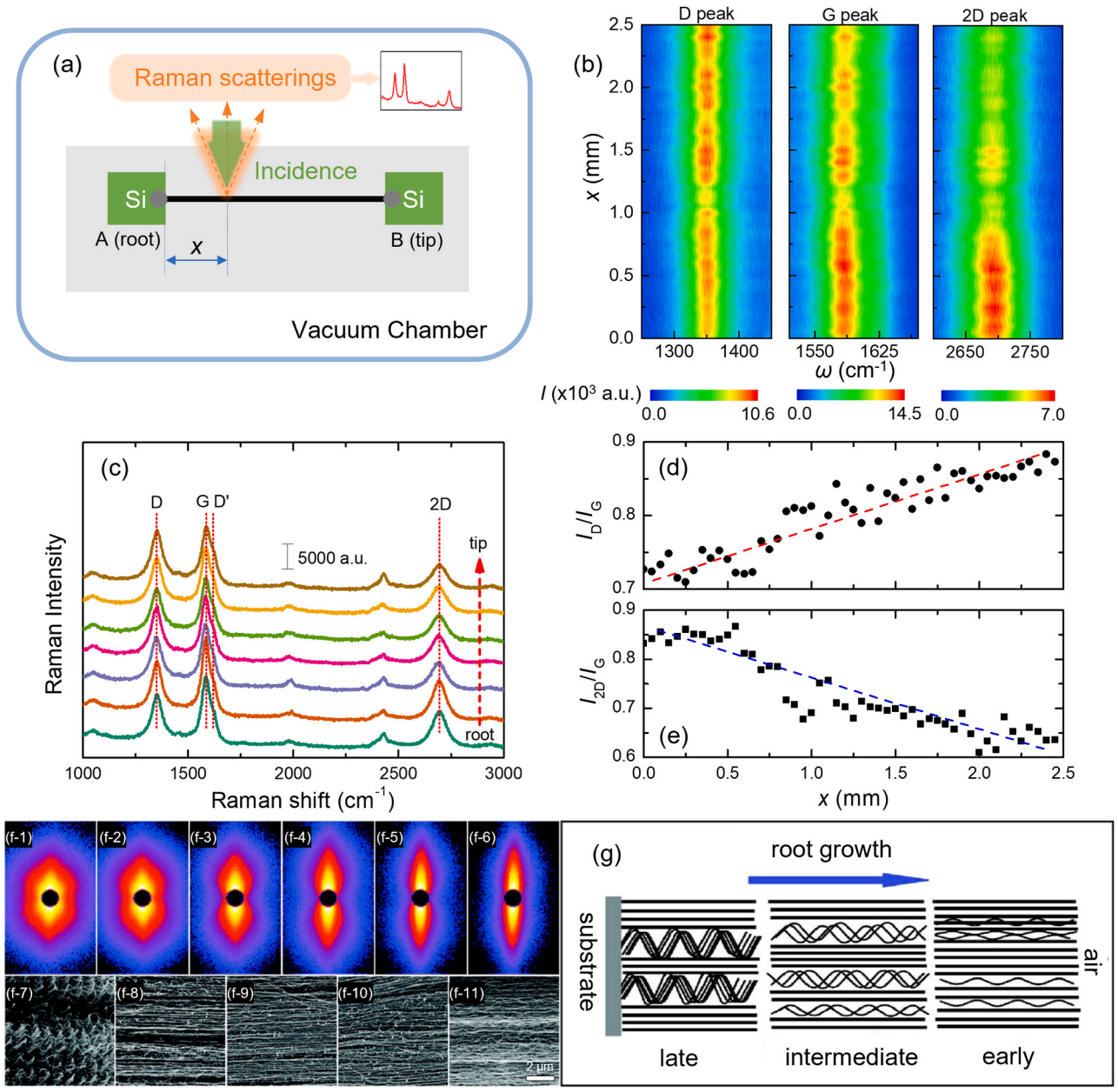

Fig. 6. Raman study of the VACNTs for structural investigation of Sample #1. (a) Schematics of the Raman mapping measurement. (b) Contour map for D, G, and 2D peaks against Raman shift and location on the bundle. (c) Raman spectra from selected locations sequentially distributed from root to tip. Changes in the intensity ratios of (d) D peak to G peak and (e) 2D peak to G peak illustrate the structural variation of the bundle from root to tip, and the dashed line indicates the varying trend. (f-1)-(f-6) are 2D small angle neutron scattering patterns of the VACNTs at different regions located from root to tip, successively. (f-7)–(f-11) are SEM images showing CNT morphology from root to tip. The scale bar in (f-11) is the same for all SEM images. (g) The schematic diagram illustrating the evolution of morphologies in VACNTs according to the root growth mechanism. [figures (f) and (g) reprinted from [42], with the permission of AIP Publishing].

Fig. 6f shows the macroscale alignment of nanotubes at different locations of a VACNTs mat reported in ref. [42]. It is obvious that two distinct CNT morphologies coexist in the VACNTs mat as well as in our sample bundle which is taken from the same mat. The order, the alignment, and the homogeneity of macroscopic nanotube assemblies vary along the growth direction of VACNTs. This is the result of the competition between collective growth of individual CNTs and spatial constraints of whole VACNTs mat. The portion of the CNTs in the tip region has more space to grow as they grow first from the catalyst film. Most of them are straight as shown in Fig. 6(f-11) and their small angle neutron scattering (SANS) pattern illustrates strong anisotropy. The negligible space between CNTs forces them to interact with each other and form a macroscopic advancing growth front. The fast growing CNTs would be suppressed by the front and have to change their growing direction and become helical or zigzag, while the slow ones could keep growing straightforward. An increasing trend of helical or zigzag morphology appears in the SEM images from Fig. 6(f-11) to (f-7). At the same time, the anisotropic feature in the SANS scattering pattern in the tip region gradually becomes isotropic in the root region [Fig. 6(f-6) to (f-1)].

Thus, for the whole bundle, the degree of structural order due to the alignment in the tip region is higher than that in the root region. The schematics in Fig. 6f adopted from ref. [42] depict the morphology in the tip, middle, and root region. As shown in the left panel of Fig. 6f, the helical or zigzag morphology is predominant in the root region which arises from random orientations of nanocrystals in most CNTs and forms

a polycrystal-like behavior rather than highly aligned structure. Though it is proved that the alignment of CNTs will not affect the Seebeck coefficient of assemblies [47], the isotropic structure, or poly-crystalline structure to be specific, at the root region renders the thermoelectric property of this portion close to *a*-C. Inoue et al. has reported that an *a*-C semiconductor exhibits p-type doped behavior and its Seebeck coefficient has a magnitude of 10^{-4} $\mu V \cdot K^{-1}$ [46] which is much higher than that of the MWCNTs in ref. [32]. Moreover, due to this poly-crystalline structure, more junctions between nanotubes arise along the axial direction (the heat and electric path direction). This has been proved to increase the Seebeck coefficient at the junctions based on theoretical simulation [35]. In contrast, most CNTs in the tip region are straight (right panel in Fig. 6f), as this portion of CNTs grew first with the least spatial constraint. Most crystals in individual CNTs at this region are well aligned along the axial direction, forming a highly-ordered assembly with strong anisotropy. Thus, the Seebeck coefficient in this region is closer to that of pure MWCNTs and lower than that in the root region. Therefore, the macroscopic alignment of VACNTs plays a more important role than the microscopic structure in individual CNTs in contributing to the thermoelectric behavior of the bundle. This results in a gradually varying local Seebeck coefficient along the VACNTs bundle. Although Fig. 6d and e show the tip region has better crystalline structure, but the local macro-scale alignment is very poor that is uncovered in Fig. 6f and g. This bad macro-scale alignment will overshadow the atomistic structure effect and significantly reduce the local thermal conductivity. Therefore, when the laser spot is irradiating the region close to the root, the heat transfer will experience a larger thermal resistance, and the resulting temperature rise is higher, as shown in Fig. 4h.

7. Conclusions

In conclusion, we have discovered photocurrent over VACNTs bundles which were taken from a CVD VACNTs mat. The photovoltage was polarized and showed similar characteristic response times to laser irradiation and Joule heating. However, since a steady voltage rise appeared over the bundle while there was no temperature difference or bias over its two ends, nonuniform local Seebeck coefficient along the bundle was proposed and proved by studying the photovoltage response under localized laser heating and scanning. It was discovered the Seebeck coefficient was not constant along the CNT bundle, rather it decreased linearly from the CNT root to tip. The origin of nonuniformity of local Seebeck coefficient arose from two possible structural factors. One is a slight increase in microscopic amorphousness and defects in individual CNTs from root to tip. The other is the obvious macroscopic structural alignment variation due to spatial interaction among CNTs during their growth. These two factors have opposite effects on Seebeck coefficient, and the macroscopic structural alignment overrides the microscopic structure effect and plays a more important role in affecting the thermoelectric property of the overall macroscopic bundle. The tailoring of the thermoelectric property of a VACNT mat by controlling its macroscopic structural alignment would be applicable to other bulks that comprise linear nanostructures and will offer a new path to manufacturing novel thermoelectric devices by taking advantage of Seebeck coefficient grading.

CRediT authorship contribution statement

S. Xu and H. Zobeiri conducted experiments and data analysis. N. Hunter and H. Zhang conducted data and structure analysis. S. Xu, G. Eres, and X. Wang conceived the concept and conducted physical model development. G. Eres did sample synthesis. All authors participated in manuscript preparation.

Declaration of Competing Interest

The authors declare that they have no known competing financial interests or personal relationships that could have appeared to influence the work reported in this paper.

Acknowledgement

Support of this work by National Science Foundation (CBET1930866 and CMMI2032464 for X.W), Program for Professor of Special Appointment (Eastern Scholar) at Shanghai Institutions of Higher Learning, and China Scholarship Council (S.X.), National Natural Science Foundation of China (No. 51876113 for S.X. and H.Z) is gratefully acknowledged. The work by G.E. was supported by the U.S. Department of Energy (DOE), Office of Science, Basic Energy Sciences (BES), Materials Sciences and Engineering Division.

References

[1] S. Iijima, Helical microtubules of graphitic carbon, Nature 354 (6348) (1991) 56–58, https://doi.org/10.1038/354056a0.
[2] R. Saito, G. Dresselhaus, M.S. Dresselhaus, Physical properties of carbon nanotubes. Imperial College Press Ed, World Scientific Publishing Co., 1998, p. 272.
[3] A. Bianco, M. Prato, Can carbon nanotubes be considered useful tools for biological applications? Adv. Mater. 15 (20) (2003) 1765–1768, https://doi.org/10.1002/adma.200301646.
[4] P. Avouris, M. Freitag, V. Perebeinos, Carbon-nanotube photonics and optoelectronics, Nat. Photonics 2 (6) (2008) 341–350, https://doi.org/10.1038/nphoton.2008.94.
[5] C. Klinger, Y. Patel, H.W.C. Postma, Carbon nanotube solar cells, PLoS One 7 (5) (2012), e37806, https://doi.org/10.1371/journal.pone.0037806.
[6] W.J. Lee, E. Ramasamy, D.Y. Lee, J.S. Song, Efficient dye-sensitized solar cells with catalytic multiwall carbon nanotube counter electrodes, ACS Appl. Mater. Interfaces 1 (6) (2009) 1145–1149, https://doi.org/10.1021/am800249k.
[7] D. Benetti, K.T. Dembele, J. Benavides, H. Zhao, S. Cloutier, I. Concina, A. Vomiero, F. Rosei, Functionalized multi-wall carbon nanotubes/tio$_2$ composites as efficient photoanodes for dye sensitized solar cells, J. Mater. Chem. C 4 (16) (2016) 3555–3562, https://doi.org/10.1039/C6TC00800C.
[8] C.P. Grigoropoulos, Laser synthesis and functionalization of nanostructures, Int. J. Extrem. Manuf. 1 (1) (2019).
[9] P.T. Mathew, F. Wang, Periodic energy decomposition analysis for electronic transport studies as a tool for atomic scale manufacturing, Int. J. Extrem. Manuf. 2 (1) (2020).
[10] M. Barkelid, V. Zwiller, Photocurrent generation in semiconducting and metallic carbon nanotubes, Nat. Photonics 8 (1) (2014) 47–51, https://doi.org/10.1038/nphoton.2013.311.
[11] K. Balasubramanian, Y. Fan, M. Burghard, K. Kern, M. Friedrich, U. Wannek, A. Mews, Photoelectronic transport imaging of individual semiconducting carbon nanotubes, Appl. Phys. Lett. 84 (13) (2004) 2400–2402, https://doi.org/10.1063/1.1688451.
[12] K. Balasubramanian, M. Burghard, K. Kern, M. Scolari, A. Mews, Photocurrent imaging of charge transport barriers in carbon nanotube devices, Nano Lett. 5 (3) (2005) 507–510, https://doi.org/10.1021/nl050053k.
[13] Y.H. Ahn, A.W. Tsen, B. Kim, Y.W. Park, J. Park, Photocurrent imaging of p−n junctions in ambipolar carbon nanotube transistors, Nano Lett. 7 (11) (2007) 3320–3323, https://doi.org/10.1021/nl071536m.
[14] A.W. Tsen, L.A.K. Donev, H. Kurt, L.H. Herman, J. Park, Imaging the electrical conductance of individual carbon nanotubes with photothermal current microscopy, Nat. Nanotechnol. 4 (2) (2009) 108–113, https://doi.org/10.1038/nnano.2008.363.
[15] B.C. St-Antoine, D. Ménard, R. Martel, Position sensitive photothermoelectric effect in suspended single-walled carbon nanotube films, Nano Lett. 9 (10) (2009) 3503–3508, https://doi.org/10.1021/nl901696j.
[16] S.J. Tans, A.R.M. Verschueren, C. Dekker, Room-temperature transistor based on a single carbon nanotube, Nature 393 (6680) (1998) 49–52, https://doi.org/10.1038/29954.
[17] X. He, X. Wang, S. Nanot, K. Cong, Q. Jiang, A.A. Kane, J.E.M. Goldsmith, R. H. Hauge, F. Léonard, J. Kono, Photothermoelectric p–n junction photodetector with intrinsic broadband polarimetry based on macroscopic carbon nanotube films, ACS Nano 7 (8) (2013) 7271–7277, https://doi.org/10.1021/nn402679u.
[18] M. Freitag, Y. Martin, J.A. Misewich, R. Martel, P. Avouris, Photoconductivity of single carbon nanotubes, Nano Lett. 3 (8) (2003) 1067–1071, https://doi.org/10.1021/nl034313e.
[19] P. Chakraborty, T. Ma, A.H. Zahiri, L. Cao, Y. Wang, Carbon-based materials for thermoelectrics, Adv. Condens. Matter Phys. (2018), 3898479, https://doi.org/10.1155/2018/3898479.
[20] G. Eres, A.A. Puretzky, D.B. Geohegan, H. Cui, In situ control of the catalyst efficiency in chemical vapor deposition of vertically aligned carbon nanotubes on

predeposited metal catalyst films, Appl. Phys. Lett. 84 (10) (2004) 1759–1761, https://doi.org/10.1063/1.1668325.
[21] Y. Xie, T. Wang, B. Zhu, C. Yan, P. Zhang, X. Wang, G. Eres, 19-fold thermal vonductivity increase of carbon nanotube bundles toward high-end thermal design applications, Carbon 139 (2002) 445–458.
[22] R. Saito, A. Grüneis, G.G. Samsonidze, V.W. Brar, G. Dresselhaus, M.S. Dresselhaus, A. Jorio, L.G. Cançado, C. Fantini, M.A. Pimenta, A.G.S. Filho, Double resonance raman spectroscopy of single-wall carbon nanotubes, New J. Phys. 5 (2003), https://doi.org/10.1088/1367-2630/5/1/157, 157-157.
[23] S. Xu, T. Wang, D. Hurley, Y. Yue, X. Wang, Development of time-domain differential raman for transient thermal probing of materials, Opt. Express 23 (8) (2015) 10040–10056, https://doi.org/10.1364/OE.23.010040.
[24] T. Wang, X. Wang, J. Guo, Z. Luo, K. Cen, Characterization of thermal diffusivity of micro/nanoscale wires by transient photo-electro-thermal technique, Appl. Phys. A 87 (4) (2007) 599–605, https://doi.org/10.1007/s00339-007-3879-y.
[25] J. Guo, X. Wang, T. Wang, Thermal characterization of microscale conductive and nonconductive wires using transient electrothermal technique, J. Appl. Phys. 101 (6) (2007), 063537, https://doi.org/10.1063/1.2714679.
[26] B. Zhu, J. Liu, T. Wang, M. Han, S. Valloppilly, S. Xu, X. Wang, Novel polyethylene fibers of very high thermal conductivity enabled by amorphous restructuring, ACS Omega 2 (7) (2017) 3931–3944, https://doi.org/10.1021/acsomega.7b00563.
[27] J. Liu, T. Wang, S. Xu, P. Yuan, X. Xu, X. Wang, Thermal conductivity of giant mono- to few-layered cvd graphene supported on an organic substrate, Nanoscale 8 (19) (2016) 10298–10309, https://doi.org/10.1039/c6nr02258h.
[28] J. Liu, Z. Xu, Z. Cheng, S. Xu, X. Wang, Thermal conductivity of ultrahigh molecular weight polyethylene crystal: defect effect uncovered by 0 k limit phonon diffusion, ACS Appl. Mater. Interfaces 7 (49) (2015) 27279–27288, https://doi.org/10.1021/acsami.5b08578.
[29] Y. Xie, B. Zhu, J. Liu, Z. Xu, X. Wang, Thermal reffusivity: uncovering phonon behavior, structural defects, and domain size, Front. Energy 12 (1) (2018) 143–157, https://doi.org/10.1007/s11708-018-0520-z.
[30] X. Huang, J. Wang, G. Eres, X. Wang, Thermophysical properties of multi-wall carbon nanotube bundles at elevated temperatures up to 830k, Carbon 49 (5) (2011) 1680–1691, https://doi.org/10.1016/j.carbon.2010.12.053.
[31] M. Tian, F. Li, L. Chen, Z. Mao, Y. Zhang, Thermoelectric power behavior in carbon nanotubule bundles from 4.2 to 300 k, Phys. Rev. B 58 (3) (1998) 1166–1168, https://doi.org/10.1103/PhysRevB.58.1166.
[32] P. Kim, L. Shi, A. Majumdar, P.L. McEuen, Thermal transport measurements of individual multiwalled nanotubes, Phys. Rev. Lett. 87 (21) (2001), 215502, https://doi.org/10.1103/PhysRevLett.87.215502.
[33] T. Miao, S. Shi, S. Yan, W. Ma, X. Zhang, K. Takahashi, T. Ikuta, Integrative characterization of the thermoelectric performance of an individual multiwalled carbon nanotube, J. Appl. Phys. 120 (12) (2016), 124302, https://doi.org/10.1063/1.4962942.
[34] Y. Nonoguchi, K. Ohashi, R. Kanazawa, K. Ashiba, K. Hata, T. Nakagawa, C. Adachi, T. Tanase, T. Kawai, Systematic conversion of single walled carbon nanotubes into n-type thermoelectric materials by molecular dopants, Sci. Rep. 3 (1) (2013) 3344, https://doi.org/10.1038/srep03344.
[35] Y. Nakai, K. Honda, K. Yanagi, H. Kataura, T. Kato, T. Yamamoto, Y. Maniwa, Giant seebeck coefficient in semiconducting single-wall carbon nanotube film, Appl. Phys. Express 7 (2) (2014), 025103, https://doi.org/10.7567/apex.7.025103.
[36] B.A. MacLeod, N.J. Stanton, I.E. Gould, D. Wesenberg, R. Ihly, Z.R. Owczarczyk, K. E. Hurst, C.S. Fewox, C.N. Folmar, K. Holman Hughes, B.L. Zink, J.L. Blackburn, A. J. Ferguson, Large n- and p-type thermoelectric power factors from doped semiconducting single-walled carbon nanotube thin films, Energy Environ. Sci. 10 (10) (2017) 2168–2179, https://doi.org/10.1039/C7EE01130J.
[37] M. Passacantando, V. Grossi, S. Santucci, High photocurrent from planar strips of vertical and horizontal aligned multi wall carbon nanotubes, Appl. Phys. Lett. 100 (16) (2012), 163119, https://doi.org/10.1063/1.4704569.
[38] S.L. Rebelo, A. Guedes, M.E. Szefczyk, A.M. Pereira, J.P. Araujo, C. Freire, Progress in the raman spectra analysis of covalently functionalized multiwalled carbon nanotubes: Unraveling disorder in graphitic materials, Phys. Chem. Chem. Phys. 18 (18) (2016) 12784–12796, https://doi.org/10.1039/c5cp06519d.
[39] H. Murphy, P. Papakonstantinou, T.I.T. Okpalugo, Raman study of multiwalled carbon nanotubes functionalized with oxygen groups, J. Vac. Sci. Technol. B 24 (2) (2006) 715–720, https://doi.org/10.1116/1.2180257.
[40] A.C. Ferrari, Raman spectroscopy of graphene and graphite: Disorder, electron–phonon coupling, doping and nonadiabatic effects, Solid State Commun. 143 (1–2) (2007) 47–57, https://doi.org/10.1016/j.ssc.2007.03.052.
[41] S. Castarlenas, C. Rubio, Á. Mayoral, C. Téllez, J. Coronas, Few-layer graphene by assisted-exfoliation of graphite with layered silicate, Carbon 73 (2014) 99–105, https://doi.org/10.1016/j.carbon.2014.02.044.
[42] H. Wang, Z. Xu, G. Eres, Order in vertically aligned carbon nanotube arrays, Appl. Phys. Lett. 88 (21) (2006), 213111, https://doi.org/10.1063/1.2206152.
[43] G. Eres, C.M. Rouleau, A.A. Puretzky, D.B. Geohegan, H. Wang, Cooperative behavior in the evolution of alignment and structure in vertically aligned carbon-nanotube arrays grown using chemical vapor deposition, Phys. Rev. Appl. 10 (2) (2018), 024010, https://doi.org/10.1103/PhysRevApplied.10.024010.
[44] G. Eres, C.M. Rouleau, M. Yoon, A.A. Puretzky, J.J. Jackson, D.B. Geohegan, Model for self-assembly of carbon nanotubes from acetylene based on real-time studies of vertically aligned growth kinetics, J. Phys. Chem. C 113 (35) (2009) 15484–15491, https://doi.org/10.1021/jp9001127.
[45] W. Weiss, W. Ranke, Surface chemistry and catalysis on well-defined epitaxial iron-oxide layers, Prog. Surf. Sci. 70 (1) (2002) 1–151.
[46] Y. Inoue, M. Sugano, S. Kawakami, M. Kitano, K. Nakajima, H. Kato, M. Hara, Electrical properties of amorphous carbon semiconductor prepared using a naphthalene precursor, BCSJ 86 (1) (2013) 45–50, https://doi.org/10.1246/bcsj.20120201.
[47] K. Fukuhara, Y. Ichinose, H. Nishidome, Y. Yomogida, F. Katsutani, N. Komatsu, W. Gao, J. Kono, K. Yanagi, Isotropic seebeck coefficient of aligned single-wall carbon nanotube films, Appl. Phys. Lett. 113 (24) (2018), 243105, https://doi.org/10.1063/1.5066021.